https://doi.org/10.5194/wes-2026-58
Preprint. Discussion started: 10 April 2026

Synthetic generation of long turbulent wind time series using hindcast model forcing for offshore wind farm simulation

Louis Pauchet[1,2], Valentin Chabaud[1], and Mostafa Bakhoday Paskyabi[3,4]
[1]SINTEF Energy Research, Postboks 4761 Torgarden, NO-7465 Trondheim, Norway
[2]INSA Rouen Normandie, 685 Av. de l'Université, 76800 Saint-Étienne-du-Rouvray, France
[3]Geophysical Institute, University of Bergen, Bergen, Norway
[4]Bergen Offshore Wind Centre, Bergen, Norway
Correspondence: Louis Pauchet (louis.pauchet@outlook.com) and Valentin Chabaud (valentin.chabaud@sintef.no)

Abstract. Offshore wind energy is crucial for the transition to a low-carbon society, and accurate modeling of turbulent wind fields is essential for the design and operation of offshore wind farms. This study aims to bridge the gap between mesoscale and microscale wind fluctuations to generate long time series that are statistically and spectrally representative of real observations, capturing the non-stationary nature of turbulence. Mesoscale data from NORA3 is combined with microscale spectra from Cheynet et al. (2018) using methodologies from Veers (1988); Sørensen et al. (2002); Chabaud (2024a) and the splicing technique introduced in Chabaud (2024b). The validation process uses observational data from the FINO1 weather mast. The model accurately reproduces the wind statistics. The along wind turbulence intensity is within a 85% confidence interval of ±0.02 for 2h simulations. The model is performing slightly better in stable conditions. The spectral representation is also good for periods between 2min and 24h. There, a mesoscale term is added to the microscale model following Larsén et al. (2013) —fitted parameters are provided— to bridge the gap between the hourly resolution of NORA3 and the typical minute-scale microscale range. The good performances and low computational needs of the presented methodology open new possibilities for the modeling of turbulence intensity, for instance for forecasting.

1 Introduction

Offshore wind energy is a cornerstone in the transition to a low-carbon society. The design and operation of offshore wind farms rely heavily on accurate modeling of turbulent wind fields to ensure structural integrity, fatigue life, and optimal power output. Traditional simulation methods typically focus on short-duration scenarios, under an hour, capturing only the microscale portion of the wind spectrum directly linked to atmospheric turbulence (Kaimal et al., 1972; Mann, 1994, 1998). Meanwhile, large-scale mesoscale models are primarily used for wind resource assessment and energy production forecasting (Solbrekke et al., 2021). Bridging this gap between mesoscale and microscale wind fluctuations to generate long time series has received limited attention until recently.

An area where modeling wind fields over longer periods is of particular interest is power fluctuations from wind farms (Sørensen et al., 2007, 2002; Chabaud, 2025) for electrical studies. There, slow but large coherent structures affecting multiple turbines play a key role. Another, less studied topic is the effect of the few but large load cycles driven by mesoscale fluctuations

https://doi.org/10.5194/wes-2026-58
Preprint. Discussion started: 10 April 2026

on fatigue damage (Sadeghi et al., 2022, 2023), that is not captured by the standard approach (International Electrotechnical Commission, 2019) using 10-min long bins which overlook the "spectral gap" leading to an underestimation of low-frequency fatigue loads. Finally, long time series are also valuable for wind farm control dealing with farm-wide (and hence mesoscale) flow processes.

As soon as mesoscale effects are taken into consideration in wind modeling, we are in the "terra incognita" of the range between the microscale and the mesoscale, as described as one of the grand challenges for wind energy science according to Veers et al. (2019), with the challenge of conserving the link between the model and the atmospheric physics. The classical representation of this range in Van Der Hoven (1957) shows a clear spectral gap but at hub height offshore more complicated behavior have been reported (Larsén et al., 2016).

The modeling of such long time series can be done using different approaches. The traditional approach known as the Veers (1988) method, essentially a Gaussian process generation based on spectrum and coherence function. Following the IEC61400-1 (International Electrotechnical Commission, 2019), the Kaimal et al. (1972) spectrum is recommended but others exist as for example introducing a low frequency mesoscale component as proposed by Larsén et al. (2013). The other approach, based on the Mann (1998, 1994) model generating a spatial wind box adding a low frequency model have been presented in Syed and Mann (2024a, b).

Recent improvement based on the Veers (1988) method include the generation of correlated wind fields at turbines points (Chabaud (2024a) in FLAggTurb), and linking the wind spectrum to atmospheric stability and friction velocity (Cheynet et al. (2018)). The latter may be resolved in large scale mesoscale model as NORA3 via SURFEX and the ECUME Scheme (Haakenstad et al., 2021; Masson et al., 2013).

This study aims to explore this "terra incognita" using these recent improvements, by combining the mesoscale and synoptic scale from NORA3 with the microscale spectrum from Cheynet et al. using the Veers, Sørensen et al. and Chabaud methodology to generate wind time series over time period of a few hours statistically and spectrally representing real observations. Along the way, this enables the modeling of turbulence intensity from mesoscale data.

In the second section, the methodology will be presented by first exposing the datasets used for mesoscale forcing and observations used for validation, then the microscale model and the novel splicing methodology will be introduced to finally expose the validation methodology. Results are compared with offshore measurement in the third section. Finally uncertainties and modeling challenges will be discussed in the fourth section.

2 Methodology

2.1 Datasets

2.1.1 NORA3

NORA3 is a high-resolution (3 km) hindcast model for the North Sea, Norwegian Sea, and Barents Sea, as represented in Figure 1 (Haakenstad et al., 2021), based on the HARMONIE-AROME prediction model (Bengtsson et al., 2017). The NORA3 model uses the 31 km ERA5 Reanalysis from Copernicus Climate Change Service (2018), described in Hersbach et al. (2020), as forcing. The high resolution, as well as good performance of NORA3 in describing the wind conditions offshore (Solbrekke et al., 2021), make it ideal as mesoscale input for wind speed, wind direction, friction velocity, and atmospheric stability.

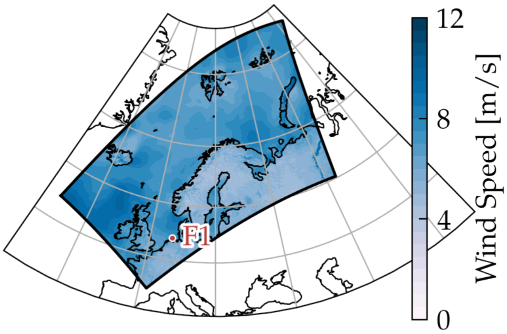

Figure 1. NORA3 Hindcast model domain (Haakenstad et al., 2021) showing for illustration the horizontal wind speed at 100 m height for July 2025. Locations of the FINO1 meteorological mast (F1) is indicated.

From the variables resolved in NORA3, it is possible to compute the Monin–Obukhov length L commonly used to estimate
60 the atmospheric stability defined as $\xi = \frac{z}{L}$, L being defined as

$$L = -\frac{u_*^3 \cdot \theta_v}{\kappa \cdot g \cdot \overline{w'\theta_v'}}, \tag{1}$$

with u_* being the friction velocity, derived from the northward and eastward momentum fluxes from NORA3, respectively $\overline{u'w'}$ and $\overline{v'w'}$, using

$$u_* = \left(\overline{u'w'}^2 + \overline{v'w'}^2\right)^{1/4}. \tag{2}$$

65 The virtual potential temperature, θ_v, is calculated from the temperature (T), pressure (P), and specific humidity (q) available in NORA3 using the relation implemented in the MetPy toolbox (May et al., 2016):

$$\theta_v = T \cdot \left(\frac{P_0}{P}\right)^{R_d/c_p} \cdot \frac{w+\epsilon}{\epsilon(1+w)}, \tag{3}$$

where $w = \frac{q}{1-q}$ is the mixing ratio, and $\epsilon \approx 0.622$ is the ratio of the gas constants for dry air and water vapor. Finally, the virtual potential temperature flux, $\overline{w'\theta_v'}$, is expressed as

70 $$\overline{w'\theta_v'} = \frac{H_{\text{sensible}}}{\rho \cdot c_p}(1 + 0.6078 \cdot q) + \left(0.6078 \cdot \theta \cdot \frac{H_{\text{lat}}}{\rho \cdot L_v}\right), \tag{4}$$

where H_{sensible} and H_{lat} are the sensible and latent heat fluxes, respectively, also available in NORA3. This derivation have been implemented in the MetOcean API toolbox from Christakos et al. (2024) to facilitate the data download as detailed in Pauchet and Chabaud (2025).

No real assessment of the modelling accuracy of surface fluxes representation has been done. It appears that the friction velocity is well represented, but the uncertain sensible heat flux tends to lead to an overly unstable representation (Pauchet and Chabaud, 2025). Addressing this uncertainty is beyond the scope of this paper, and the above-presented hourly wind conditions from NORA3 are used as is in the configuration of the microscale model described in 2.2.1.

2.1.2 FINO1

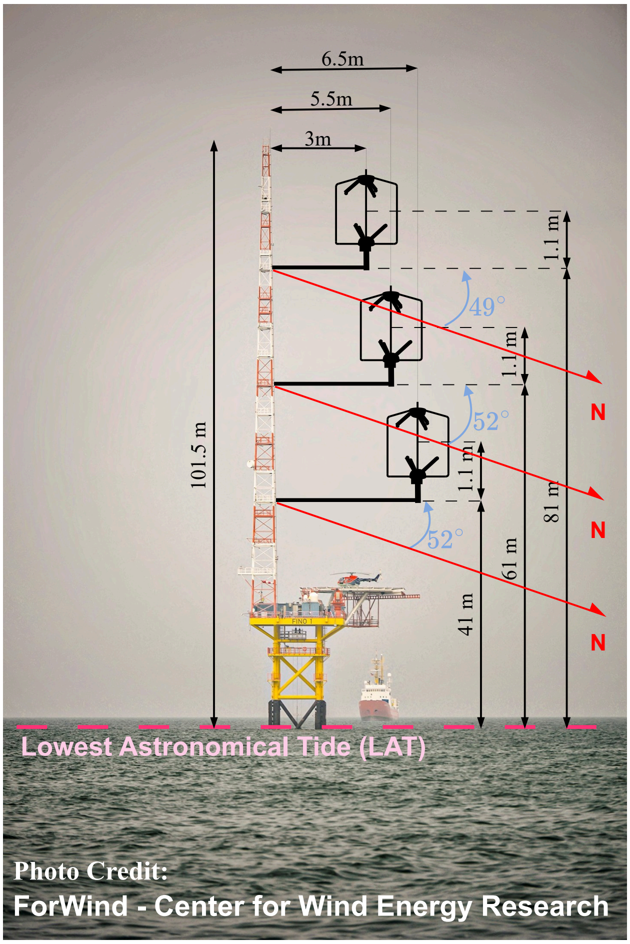

Photo Credit:
ForWind - Center for Wind Energy Research

Figure 2. Picture of the FINO1 Platform with the position of the three Gill R3-50 Sonic Anemometers. The red arrow represent the 0° North heading.

In the validation process presented later, we will use observational data from the FINO1 weather mast, located 45 kilometers north of Borkum (Germany) within the Alpha Ventus wind farm ($N\,54°00'53.5''$, $E\,006°35'15.5''$), as shown in Figure 1. The platform consists of a square lattice mast reaching 101 m above the lowest astronomical tide (LAT), built on a 20-m high jacket. Among other sensors, the tower is equipped with three Gill R3-50 sonic anemometers sampling at 10 Hz, mounted on booms at 41, 61, and 81 m above LAT and measuring at 42.1, 62.1, and 82.1 m, respectively (Bundesamt für Seeschifffahrt und Hydrographie (BSH), 2015). The mast and the positions of the sonic anemometers are illustrated in Figure 2; the 41 m and 61 m sonics are heading to 308° and the 81 m to 311°.

We used the processed data to compute the atmospheric stability, friction velocity, and wind components for 10-min periods from Pauchet et al. (2025). In this dataset, fluxes are processed with EddyPro (Fratini and Mauder, 2014; LI-COR Biosciences, 2021) using the standard configuration with double rotation for tilt correction and covariance maximization for time lag correction, as described in LI-COR Biosciences (2023). The 10-min wind components are computed to follow the notation of Kaimal and Finnigan (1994), maximizing the along-wind component u so that the average of the side-wind component v is negligible. This approach has also been applied to obtain the 1-min average wind components from the raw measurements. Processing details are provided in (Pauchet and Chabaud, 2025). From the original dataset, high-frequency filtering using a 4th-order Butterworth low-pass filter with cutoff set to $f = 0.125$Hz corresponding at the highest frequency simulated in microscale synthetic turbulence generation (see Sec. 2.2.2).

The wind speed, wind direction and friction velocity have been filtered to be in range of interest for wind turbine application as presented in Table 1. The atmospheric stability range has been limited to $z/L \in [-2,2]$ as conditions outside this range may be considered as extreme. We only considered data where the quality check for wind speed and direction were lower than two (see Pauchet et al.; Pauchet and Chabaud for the detail) and where the quality check for sensible and momentum fluxes was lower or equal to 1 according the classification of Foken et al. (2005). Finally, the data has been filtered to reduce the impact of the mast distortion by removing a sector of 40° centered on the 131° bearing for the highest sonic, and by only using data acquired before the construction of the wind farm (around 2009).

2.2 Time serie generation

2.2.1 Microscale Model

The standard IEC 61400-1 (International Electrotechnical Commission, 2019) defines the turbine design specifications and recommends using the wind turbulence model from Mann (1998, 1994) or from Kaimal et al. (1972) (designated hereafter as the Kaimal et al. spectrum). The latter model is commonly used for offshore turbine design, as integrated in the code TurbSim (Jonkman, 2009), but it has the major limitation of being based on onshore observations and thus not accounting for atmospheric stability. Therefore, the model from Cheynet et al. (2018) (designated as the Cheynet et al. spectrum) has been used for the u component, while the v and w components follow the Kaimal et al. spectrum.

This model is designed to represent the wind spectrum for periods up to one hour using the spectral form designated as "point-blunt" model with four parameters a_1^u, b_1^u, a_2^u and b_2^u, as follow

$$\left(\frac{nS_u}{u_*^2}\right)_{\text{micro}} = \frac{a_1^u \cdot f}{(1+b_1^u \cdot f)^{5/3}} + \frac{a_2^u \cdot f}{1+b_2^u \cdot f^{5/3}} \tag{5}$$

where u_* is the friction velocity and $f = nz/\overline{u}$ the reduced frequency with z the elevation and $\overline{u}$ the average along wind speed for the considered averaging period. This spectrum is ideally adapted for neutral condition but is also used in unstable and stable stratification (Cheynet et al., 2018). In stable conditions, following Smedman-Högström and Högström (1975), the spectral gap should usually be visible in spectra covering periods lower than one hour. To this end, a mesoscale component is added to the spectrum using the formula proposed by Larsén et al. (2013)

$$\left(\frac{nS_u}{u_*^2}\right)_{\text{meso}} = a_3 f^{-2} + a_4 f^{-2/3}. \tag{6}$$

Cheynet et al. assume that the mesoscale fluctuation is dominating the turbulence in stable condition giving the following simplified expression

$$\frac{nS_u}{u_*^2} = c_1 f^{-2/3} + \frac{a_2^u \cdot f}{1+b_2^u \cdot f^{5/3}} + a_3 f^{-2}. \tag{7}$$

on which parameters have been fitted.

The normalization follows the principles of the Monin-Obukhov Similarity Theory, hence parameters should only depend on atmospheric stability, as shown by Cheynet et al.. The fitted parameters are provided in their Table 3 Appendix 1.

2.2.2 High-frequency Wind Simulation with Gaussian Process Model

To generate time series from the Cheynet et al. spectrum, we employ a correlated Gaussian process model based on the method described by Veers (1988) implemented in a fork of TurbSim, FLAggTurb —Farm-Level Aggregated Turbulence— by Chabaud (2024a, 2023). This approach allows the generation of multiple realizations with different seeds to ensure independent time series and can be applied to generate 2-hour wind time series for each unique case of wind speed, wind direction, atmospheric stability, and friction velocity in the range and increment presented in Table 1, giving the microscale part of the wind spectrum.

The power of FLAggTurb lies in its ability to aggregate the spectrum over the rotor area, enabling fully-correlated (including lifting Taylor's frozen-turbulence assumption) synthetic turbulence generation over large wind farms. There, the coherence model developed by Vigueras-Rodríguez et al. (2012) is used, resolving the farm-level mesoscale coherence based on measurements from the turbines of the Nysted wind farm in the Baltic Sea. The focus of this study is on the one point wind spectrum part, and for this purpose the widest spectrum possible is used for comparison with observations. To this end, a 1m diameter rotor is used as basis for aggregation, removing its low-pass filtering effect. This works also serve as validation of the implementation of a part of FLAggTurb.

Regarding time resolution, the 2-hour duration is crucial to obtain a consistent evolution of turbulence on top of hourly weather data, as shown in Sec. 2.2.3. A sampling interval of 1s is chosen with a highest simulated frequency of 0.125Hz yielding minimum 8 points per period.

Table 1. Unique mesoscale condition used as input for simulations

Parameter	**Range**	**Increment**
Wind Speed	3 to 25 m/s	1 m/s
Wind Direction	0 to 360 °	5°
Friction Velocity ($u_\star$)	0 to 1.4 m/s	0.1 m/s
Parameter	**Bins**	
Stability (z/L)	$[-2,-1,-0.5,-0.2,0.2,0.5,1,2]$	

2.2.3 Spectral Splicing Method

Mixing the microscale model with hourly mesoscale hindcast data is not straightforward and necessitates a novel method aligned with Gaussian process generation presented in the following, with more details in Chabaud (2024b). We start from the mesoscale slowly-varying wind speed, and seek to add microscale fluctuations described by a continuously evolving spectrum derived from mean wind conditions (friction velocity u_*, stability z/L, wind speed U, and direction φ) from mesoscale data.

To each mesoscale time step (one hour, represented in red triangle in Figure 3) is attributed one realization of two-hour turbulent wind field data that should smoothly transition from the previous step and to the next one, with the following requirements:

- Continuous temporal crossfade to ensure there is no discontinuity in the time series;
- Linear transition between the power spectral densities of the successive wind fields;

We will call this process splicing, with a mathematical description showed in the following.

Let $x'_1(t)$ and $x'_2(t)$ be the fluctuating parts of two consecutive wind fields overlapping in $[t_0, t_0 + 1\,\mathrm{h}]$, where t_0 is any time step of the mesoscale time series, and simplify the notation to $[t_0, t_0 + 1\,\mathrm{h}] = [0, T]$. $\overline{x}_{m,1}$ and $\overline{x}_{m,2}$ stand for the respective average values, $y'(t)$ for the resulting spliced fluctuation and $\overline{y}(t)$ for its moving average. x may represent any wind speed component (u is used for illustration in Figure 3).

Starting with a linear crossfade defined as

$$y'(t) = \begin{cases} x'_1(t), & t < 0, \\ (1-\alpha(t))x'_1(t) + \alpha(t)x'_2(t), & 0 \le t \le T, \\ x'_2(t), & t > T, \end{cases} \tag{8}$$

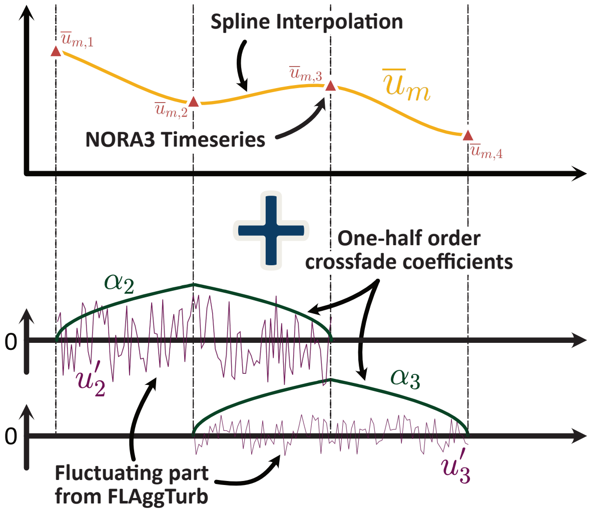

Figure 3. Illustration of the splicing process merging the spline interpolated average from NORA3 with the high frequency fluctuations of FLAggTurb. u is used as an example fo specific variable instead of the general x used in the text.

This linear crossfade is not suited to transition the fluctuating part as the power spectral density would be expressed as

$$\begin{aligned}S_{yy}(f,t) = &\underbrace{(1-\alpha(t))^2 S_{x_1x_1}(f)}_{x_1 \text{ contribution to the PSD}} + \underbrace{\alpha(t)^2 S_{x_2x_2}(f)}_{x_2 \text{ contribution to the PSD}} \\ &+ \underbrace{2(1-\alpha(t))\alpha(t)\Re\{S_{x_1x_2}(f)\}}_{\text{cross-contribution of } x_1 \text{ and } x_2}\end{aligned} \tag{9}$$

which do not satisfy the condition of linear transition between the PSD of the different signals. To solve this we need to use the square root of the linear crossfade to adjust the amplitude.

Therefore, the crossfaded signal is constructed as

$$y'(t) = \sqrt{1-\alpha(t)}\,x'_1(t) + \sqrt{\alpha(t)}\,x'_2(t). \tag{10}$$

The PSD of $y(t)$ then becomes

$$\begin{aligned}S_{yy}(f,t) = &(1-\alpha(t))S_{x_1x_1}(f) + \alpha(t)S_{x_2x_2}(f) \\ &+ 2\sqrt{(1-\alpha(t))\alpha(t)}\,\Re\{S_{x_1x_2}(f)\}\end{aligned} \tag{11}$$

To fulfill the objective of linear transitions between PSDs, the cross corelation term $2\sqrt{(1-\alpha(t))\alpha(t)}\,\Re\{S_{x_1x_2}(f)\}$ must be zero when averaged over statistical realizations. This is achieved by (1) picking up among time series generated with different seeds (presented in 2.2.2), and (2) repeating this process with random combinations of seeds. This yields a set of independent long time series, see Chabaud (2024b) for a mathematical proof. Results using these long time series should then be averaged over realisations (i.e. Monte Carlo simulations consistently with Gaussian process generation).

Finally, as $\overline{y(t)} \approx 0$ by construction, we must add the slowly-varying (mesoscale) part of the signal. The interpolation used for the mesoscale signal must ensure the continuity of both the series and its derivatives to avoid introducing high-frequency artifacts. A third-order spline interpolation is used, designated as $y_m(t)$, yielding the final relation:

$$y(t) = \sqrt{1-\alpha(t)}\, x_1'(t) + \sqrt{\alpha(t)}\, x_2'(t) + y_m(t) \tag{12}$$

2.3 Validation of the Model

Due to the stochastic nature of the generation process, direct temporal comparison of high-frequency time series is not meaningful. Instead, the validation focuses on two key aspects: the 10-minutes statistics (mean for the along-wind component and standard deviation for all three components) and the spectral representation of the signal. These steps are detailed below.

2.3.1 Statistical Validation

The generated time series, sampled at 1 Hz, are resampled using the capabilities of Xarray (Hoyer and Hamman, 2017) to compute both 10-minute and 1-minute statistics. The 10-minute statistics are directly comparable to the filtered FINO1 data presented in 2.1.2, while the 1-minute statistics are used for spectral analysis. For clarity, the 10-minute statistics are further averaged into hourly steps to visualize month-long time series effectively.

To quantify the error of the method, the mean bias error (MBE) and the root mean square error (RMSE) are employed. One of the key values is the turbulence intensity (TI_k) so the error will be calculated on it. TI_k is computed as

$$TI_k = \frac{\sigma_k}{\overline{u}}, \quad k \in \{u, v, w\} \tag{13}$$

The MBE and RMSE will be defined as

$$\text{MBE} = \frac{1}{N}\sum_{i=1}^{N} y_i - \hat{y}_i, \tag{14}$$

and

$$\text{RMSE} = \sqrt{\frac{1}{N}\sum_{i=1}^{N} (y_i - \hat{y}_i)^2}, \tag{15}$$

where y_i and $\hat{y}_i$ represent the observed and predicted values, respectively, and N is the number of observations. In our case, y can represent any of the values in the generated time series, including TI_u, TI_v, TI_w (the 10-minute turbulence intensity of the signal).

When computing the error, there are two approaches: (1) over the entire dataset to compute the absolute metrics, or (2) over short periods of a few hours. The first approach is useful for estimating the overall average error of the method, while the second approach is beneficial for estimating the confidence interval of a generated signal over shorter periods of 2 hours, grouping up to 12 data points.

2.3.2 Spectral Validation

The spectral validation step will focus on the part of the spectrum that directly depends on weather conditions; thus, the well-understood inertial range (i), as defined in Högström et al. (2002), is not of primary interest. (The boundary layer turbulence range (i - iii) and the mesoscale turbulence range (iv) are illustrated in Figure 4.) However, it is interesting to observe the connection between the mesoscale (iv) and the low-frequency range (iii), and potentially the self-similar range (ii), as mesoscale behavior can impact relatively high frequencies in stable conditions according to the work of Kaimal et al. (1972). Larsén et al. (2016) observed that the ranges (ii) and (iii) of interest are not easily distinguishable and that the spectral gap is not clearly marked offshore at heights corresponding to turbine rotors. The absence of a clear spectral gap underscores the importance of the presented splicing methodology, as traditional methods relying on scale separation fail in such cases.

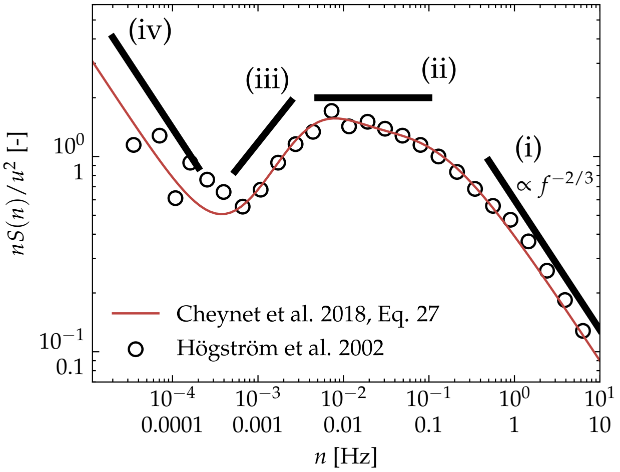

Figure 4. The spectral ranges described in Högström et al. (2002): (i) the Kolmogorov inertial range, (ii) the surface eddy or self-similar range, (iii) the low-frequency range, and (iv) the mesoscale range.

The effect of height on these ranges, as demonstrated by Högström et al. (2002), extends the inertial sub-range to lower frequencies due to reduced distortion of eddies from surface interaction. At wind turbine hub height, assuming the height remains within the eddy surface layer[1], the ratio n_u/n_l would be close to 1 (where n_u and n_l are the upper and lower frequencies of the self-similar range). This implies that the self-similar range would be on a narrow band. We can estimate n_l using Högström

---

[1] While the eddy surface layer, typically $1/30$ of the atmospheric boundary layer (ABL), corresponds to a height of 30–60 m for an ABL of 1–2 km, well below the hub height of offshore turbines (above 100 m), this assumption provides a conservative upper bound for the frequency limits of our analysis.

et al. as $n_l \approx f_c \cdot \frac{\overline{u}}{u_*} \cdot \frac{1}{0.2 \times 0.047 \cdot z}$. Using the average values at FINO1 for 2007–2008, where $\frac{\overline{u}}{u_*} \approx 34$, we find that at $z = 81$ m, $\frac{1}{n_l} \approx 1.2 \times 10^3$ s (approximately 20 minutes). These time periods are typically dominated by mesoscale effects, especially in neutral and stable stratification. Therefore, using 1-minute resampled data, we expect to observe phenomena within range (iii) and potentially range (ii), n_u being typically around 10^{-1}–10^{-2}Hz, in addition to the mesoscale range (iv). The resampling have been applied using a block average after verifying that this would not impact the spectrum with aliasing.

The normalization used by Cheynet et al. lacks meaning outside the microscale range, therefore for validation the raw unnormalized spectra will be used to compare simulations and observations. To validate spectra between 2-min to 24h period, the time series have been split in 24h chunks. For each chunk, eventual missing values have been interpolated using Piecewise Cubic Hermite Interpolating Polynomial (PCHIP) to avoid sharp change and ensure continuity in the first-order derivative. If more than 25% of the values are missing, the chunk is discarded.

The spectra are then computed using the Welch method with a single hamming window for 24h and using zero padding to 5 times the number of points available in the chunk (nfft = 5) to ensure enough spectral points in the low frequency. Then to reduce the variance of the spectra, the same "log-smoothing" or "log-averaging" methodology as Cheynet et al. or Larsén et al. will be applied using 50 points per decade.

3 Results

To mitigate stochastic uncertainty while maintaining computational efficiency, we generated an ensemble of five independent realizations for each microscale state and three realizations (different combinations of microscale realizations) of the aggregated long-term series are generated, processed and averaged over those three independent seed combinations.

3.1 Statistical representation

Figure 5 shows the distribution of $\overline{u}$ (panel A), σ_u (panel B), σ_v (panel C), and σ_w (panel D) between the measurements at 81 m at FINO1 and the generated time series at 100 m. Additionally, panels E and F represent the wind direction and the friction velocity u_*, respectively, as obtain directly from NORA3.

Starting with NORA3, we observe good agreement between the two distributions for the friction velocity as of Figure 5F. This is important as an accurate representation of friction velocity is crucial for microscale generation using the Cheynet et al. spectrum. The wind direction distribution depicts a slight offset, reasonably attributed to a misalignment of approximately 30° in the FINO1 dataset processing, likely due to a calibration issue. A significant share of uncertainties is associated with unstable conditions where NORA3 appears to be overly unstable compared to the observations at FINO1, due to an erroneous sensible heat flux as introduced in Sec. 2.1.1.

In the defined range of wind speeds $[3, 25]$ m/s, the distributions for mean wind speed appear similar for when $\overline{u} > 9$m/s. For lower wind speeds, the generated time series seem to overestimate $\overline{u}$ compared to observational data. It would be expected to find a similar distribution than Solbrekke et al. (2021) who found that NORA3 slightly underestimate the wind speed at FINO1

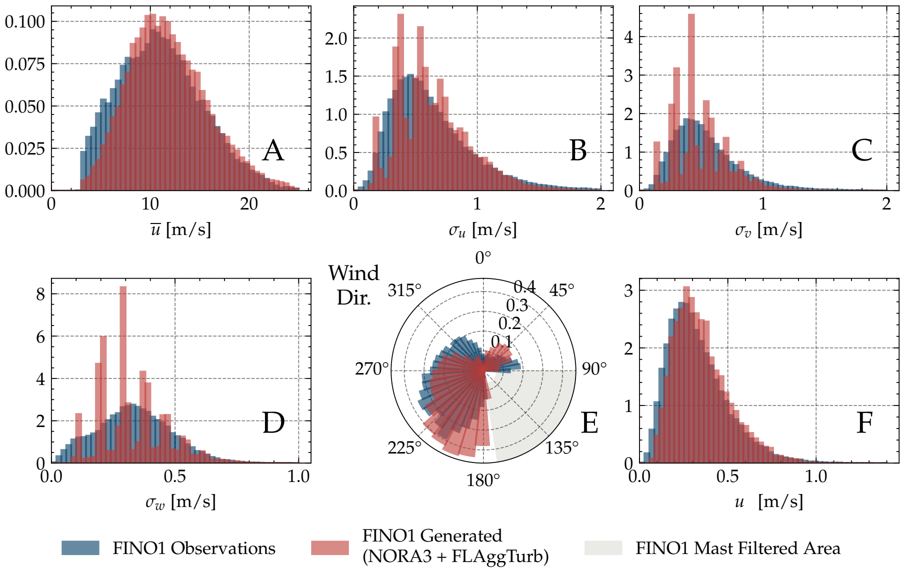

Figure 5. Comparison at 81 m ALAT at FINO1 for 2007–2008 of the distribution of (A) along-wind speed u, (B) standard deviation of the along-wind component σ_u, (C) standard deviation of the side-wind component σ_v, (D) standard deviation of the vertical wind component σ_w, (E) wind direction, and (F) friction velocity u_*

at low wind speed. In this case, a major source of systematic vertical shear bias would be the difference between the generation height (100m) and the observation height (81m).

Additionally, it is expected to have the generated data picturing a distribution showing slightly higher wind speed as the the generated data are higher up (100m) than the observations (81m).

Perhaps most interesting is the modeling of standard deviations (and hence turbulence intensities), whose distributions are presented in Figures 5B, C & D. An excellent agreement between the observations and the model is observed for the σ_u component in highly fluctuating flows. At lower fluctuations, battlement in the distribution is observed, which is attributed to the binning resolution for friction velocity and atmospheric stability which directly drive the generation of the fluctuations. Overall, those battlements would compensate using larger bins for the distribution.

The σ_v and σ_w component also shows similar and rather large battlement which led to a density difference, especially at high fluctuation conditions potentially linked to the discretizations of the mesoscale data. Those shift also underline a general underestimation of the fluctuation for the σ_v and σ_w component which, especially for σ_w is also visible on the time series presented Figure 6D. This underestimation is likely linked to the absence of large-scale lateral wind fluctuation estimates in NORA3, which, due to its limited resolution, fails to capture sub-grid scale (SGS) variance, especially in the lateral (v) and vertical (w) components, both of which are more sensitive to local surface roughness and atmospheric stability than the longitudinal component.

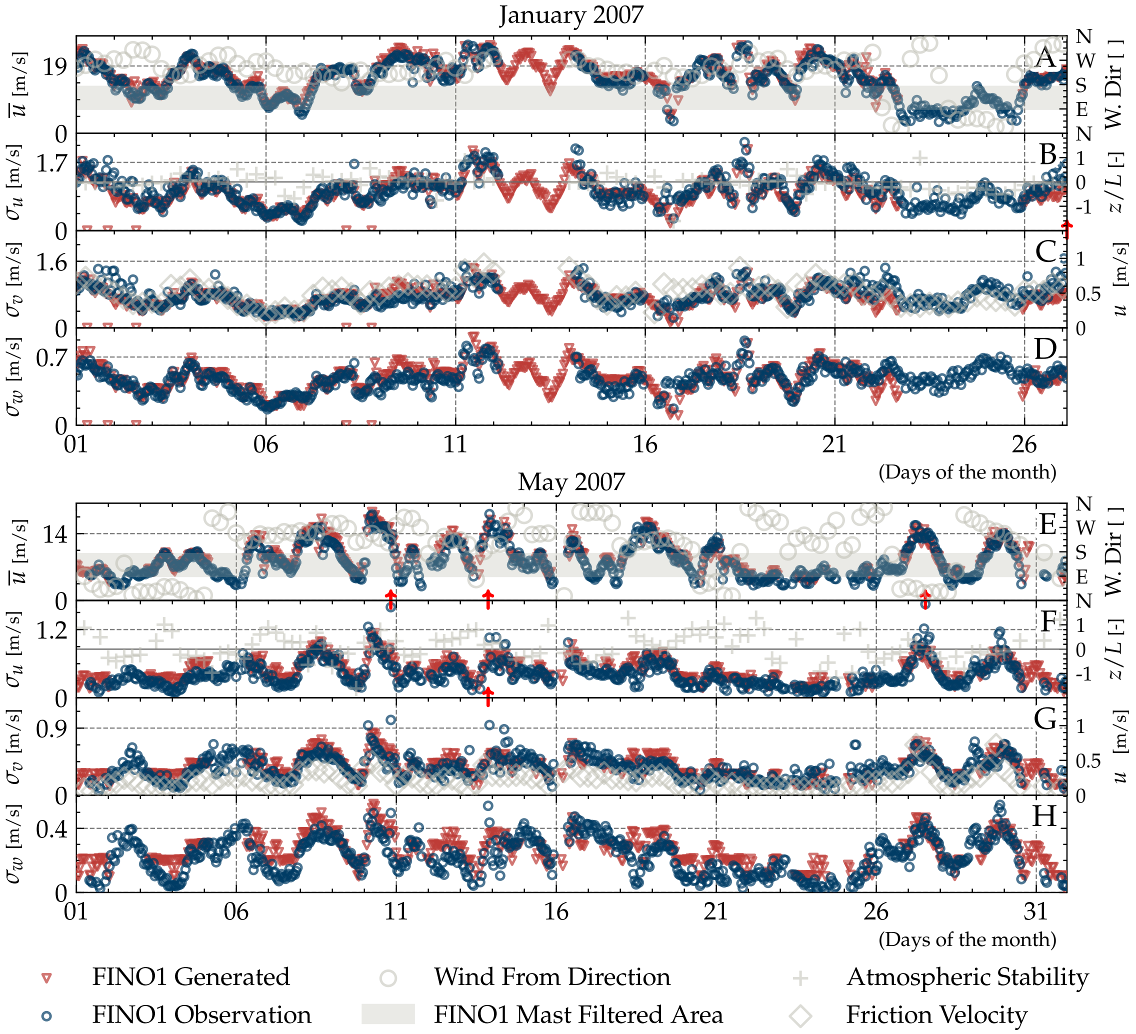

Figure 6. Comparison at 81 m ALAT at FINO1 for January (A–D) and May 2007 (E–H) of (A & E) $\overline{u}$, (B & F) σ_u, (C & G) σ_v, and (D & H) σ_w. The statistics are computed on 10-minute intervals before being averaged over 3 seeds and then averaged over 1-hour periods for representation. The red arrows indicate values exceeding 5σ, the y-axis upper limit.

The time series for $\overline{u}$, σ_u, σ_v and σ_w are presented in Figure 6 for January 2007, which features the highest wind speed and TI for 2007-2008, and for May 2007, which features the lowest wind speed and TI for the same period. For the overall period where data is available, we can observe an excellent temporal agreement of the 1-h average of 10-min statistics averaged over 3 seeds. The seed averaging is necessary for temporal comparisons as 10-min statistics still contain realization-dependent stochastic variations (consistently with Gaussian process generation).

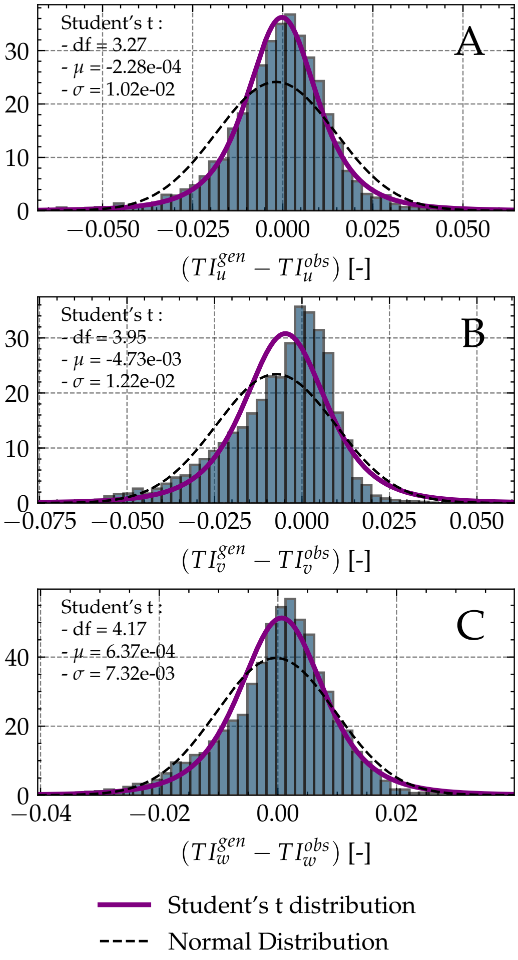

Figure 7. Distribution of the mean error (ME) of TI_u, TI_v, and TI_w, and fitted student's t law with resulting hyperparameters.

As seen on the distribution in Figure 6D, at high TIs the model is underestimating the vertical fluctuation.

For those two months, the wind direction was mostly from north to south and the atmospheric stability overall stable or near neutral with some short unstable or very unstable time periods.

After this overview, it is worth noting that for multiple events, fluctuations are for short periods of time much higher than the generated time series (see 10, 14 and 29 May 2007 or 18 and 21 January 2007). This highlights the so-called "extreme events" where fluctuations are much higher than expected that have been filtered out from the Cheynet et al. microscale model and are complicated to resolve.

We can also observe sporadic zero-fluctuation points (as in early January) which contributes to the general uncertainty of the method, presented in the following.

Table 2. Mean error statistics for the turbulence intensity based on 2h error averaging.

	TI_u	TI_v	TI_w
Q25	-0.00869	-0.0155	-0.00486
Q50	-0.0001	-0.0034	0.00089
Q75	0.00722	0.00389	0.00572
CI 85%	[-0.020, 0.019]	[-0.027, 0.017]	[-0.013, 0.014]
CI 95%	[-0.032, 0.031]	[-0.039, 0.030]	[-0.020, 0.021]
CI 99%	[-0.056, 0.055]	[-0.062, 0.052]	[-0.033, 0.034]

CI = Confidence Interval computed on a student's t distribution as in Figure 7;
Q = Percentile

Figure 7 shows the distribution of the mean bias error on the turbulence intensity $TI_k = \sigma_k/\overline{u}, k \in [u, v, w]$, computed over 2-hour time periods representing a maximum of 12 data points (fewer if data is missing). A normal distribution and a Student's t-distribution have been fitted to the data, with their parameters provided in the figure. As visible in Figure 7, the normal distribution does not properly represent the data, whereas the Student's t-distribution provides a much better fit.

First of all, the error distribution is mainly centered on zero with an average of the fitted distribution -2.28×10^{-4} and -4.73×10^{-2} for the u and v respectively. This would highlight a negative bias indicating that the generated time series would underestimate the turbulence intensity in average for u and v while overestimating it for w as a positif bias of 6.37×10^{-4}. This bias correspond to less than 1% of turbulence intensity yielding a good accuracy of the 2h estimation of the turbulence intensity.

The spread of the distribution is relatively low, with more than half of the error measurements falling within the intervals $[-0.009, 0.008]$, $[-0.02, 0.004]$, and $[-0.005, 0.006]$ for the turbulence intensity components u, v, and w, respectively. These intervals are defined by the first (Q25) and third quartiles (Q75), as presented in Table 2. Additionally, this table provides the confidence intervals at 85%, 95%, and 99% levels, both in general and per atmospheric stability, as illustrated in Figure 8. These confidence intervals are based on the distribution presented in Appendix A, Figure A1.

The 85% confidence interval for the error associated with 2-hour generation using the provided methodology is $[-0.02, 0.02]$ for the u component of turbulence intensity.

As expected from the known overly unstable behavior of NORA3, the uncertainties in unstable conditions are higher leading to a wider confidence interval in Figure 8. Best performance is observed in neutral conditions, followed by stable and unstable conditions. Another factor of uncertainty to consider is the spectral gap between NORA3's Nyquist frequency and the microscale range, as the model from Cheynet et al. (2018) does not include a mesoscale component in unstable and neutral conditions.

The lower uncertainties for the neutral case for the v and w component may be attributed to the use of the Kaimal spectral model for these components in FLAggTurb, model being appropriate in neutral conditions.

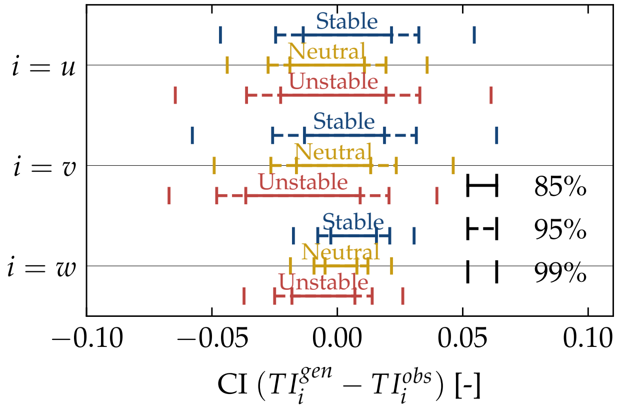

Figure 8. Confidence intervals at 85%, 95%, and 99% for unstable ($z/L \in]-2,-0.1]$), neutral ($z/L \in]-0.1,0.1]$), and stable ($z/L \in]0.1,2[$) conditions, derived from the Student's t distribution of Figure 7

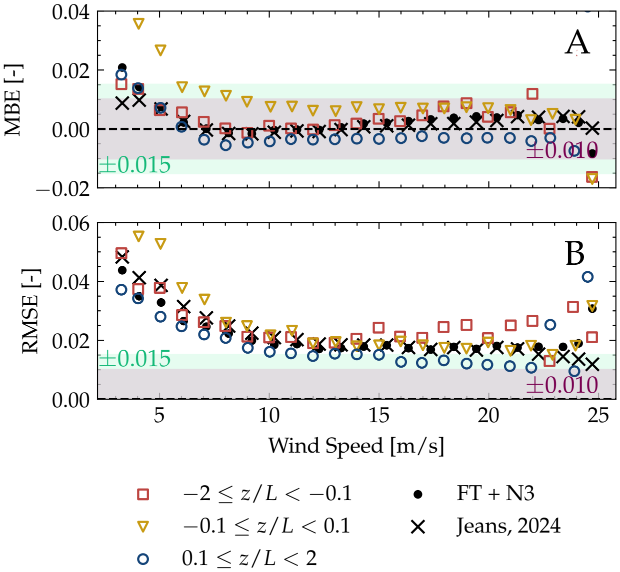

Figure 9. (A) Mean Bias Error (MBE) and (B) Root Mean Square Error (RMSE) for $TI_u = \sigma_u/\overline{u}$ over different wind speed bins and atmospheric stability for 2007-2008 at FINO1

Finally, we can examine the performance of the developed methodology as a function of atmospheric stability and wind speed, as presented in Figure 9. There, the averages of the MBE and the RMSE are displayed per bin of wind speed along with the ±0.010 and ±0.015 ranges as provided by the standard for wind sensors systems for offshore wind energy (IEC 61400-50 serie).

Regarding the MBE (Figure 9A) which estimates the accuracy of the methodology, it is within the acceptable range in average for wind speeds higher than 5 m/s as well as in stable and unstable conditions. For neutral conditions, the MBE is slightly higher than the acceptance range, even higher than in unstable conditions, which contrasts with the previous error estimation method. The accuracy of the suggested method outperforms Lidar accuracy as presented by St. Pé et al. (2021). who showed a MBE in the range $[0.006, 0.024]$ for wind speeds between 4 and 12 m/s, versus $[-0.0016, 0.0142]$ for the suggested method on the same wind speed range.

The second metric used is the root mean square error, which evaluates the precision and appears to be above the defined acceptance range except for stable conditions at wind speeds higher than 10 m/s. Again, the neutral condition depicts a lower precision at low wind speeds than the other conditions and the global series. Comparing with the precision from Lidar measurements in St. Pé et al. (2021) on the same speed range as above, $RMSE_{TI}^{[4,12]} \in [0.022, 0.057]$ was obtained, versus $RMSE_{TI}^{[4,12]} \in [0.018, 0.035]$ here, showing again slightly better performances.

For both metrics, the performances are similar to the extended ISO model based on ISO19901-1:2015 (ISO, 2015) developed by Jeans (2024) as shown Figure 9.

3.2 Spectral representation

Figure 10 presents the pre-multiplied ($nS_u(n)$) along-wind (u) spectrum for 3 stability categories from unstable ($z/L \in [-2, -0.1[$), neutral ($z/L \in [-0.1, 0.1[$) and stable ($z/L \in [0.1, 2[$) at FINO1 for the period 2007-2008. Observations from the sonic anemometer at 81.5m are represented by blue circles, whose general trend fits with the full-scale spectra proposed by Larsén et al..

In red triangles is presented the wind spectrum generated by combining the NORA3 hindcast and the Cheynet et al. model, used in the statistical representation result. A general good agreement can be observed in the mesoscale spectrum up to a period of two hours (1.4×10^{-4}Hz), where in stable and neutral conditions we observe a drop in spectral density as the Nyquist frequency of NORA3 is reached and there is no mesoscale component in the spectrum proposed by Cheynet et al. for unstable and neutral. In the stable case, the opposite behaviour —a bump in PSD— is observed as the mesoscale component form Cheynet et al. only takes into account the high-frequency part of mesoscale fluctuations.

To solve this issue, the Cheynet et al. model was modified by introducing a mesoscale component based on Larsén et al. (2013) following $fS_u(f) = a_3 f^{-2/3} + a_4 f^{-2}$ on all stability classes, also replacing the mesoscale component in stable case. The parameters a_3 and a_4 have been fitted on the observed spectrum and displayed in red line on the Figure 10.

The spectrum generated based on these new mesoscale parameters is represented by yellow triangles in Figure 10. There, we observe a much better agreement between the observed spectra and the generated spectra especially in the range 2h (1.4×10^{-4}Hz) to 30min (5×10^{-4}Hz) periods.

From the higher frequency part, from 20min (8×10^{-4}Hz) to the Nyquist frequency from using 1-min resample time series, the microscale is properly represented in the intermediate frequency range, though with an overestimation of the pre-multiplied power spectral density in stable conditions. The inertial sub-range being well understood and this study being about bridging

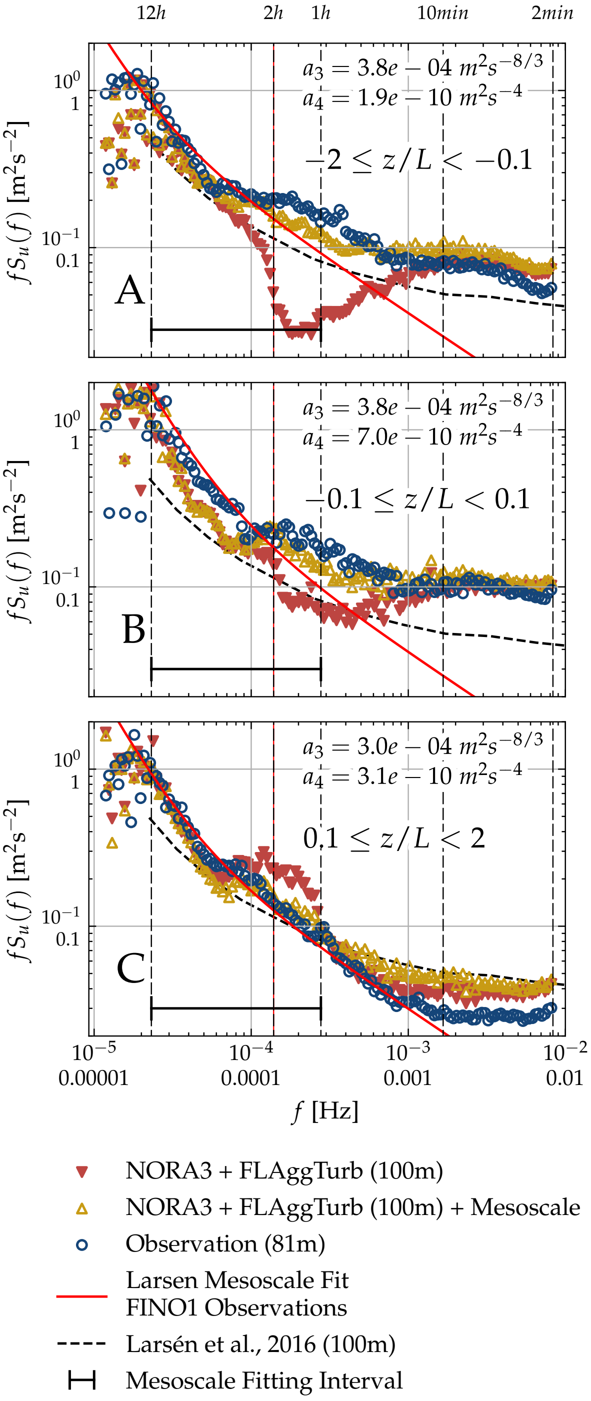

Figure 10. u-component of the wind spectrum at FINO1 for the period 2007-2008 in (A) unstable, (B) neutral and (C) stable conditions. The blue circles represent the observation at FINO1 81.5m, the red triangles correspond to the generated time series without the model of Cheynet et al. (2018) and the yellow triangle yellow the generated time series with the fitted a_3 and a_4 on the mesoscale of FINO1. The black and red line at 2h represent the Nyquist frequency of NORA3.

microscale and mesoscale, it has not been represented, especially because of the complexity of dealing with very high frequency data.

4 Discussion

4.1 On turbulence intensity

As described in the results, uncertainties in turbulence intensity calculations are important and need to be discussed.

First of all, uncertainties exist in the hindcast model use as forcing for the presented method, NORA3, as described by Solbrekke et al. (2021). What was not part of their study correspond to the surface fluxes used as input for the microscale Cheynet et al. model. This has been part of the work of Pauchet and Chabaud, where it was found that the representation of the friction velocity u_* is globally good at FINO1 but the error on the regression slope of the sensible heat flux lead to a bad estimation of the atmospheric stability in unstable conditions.

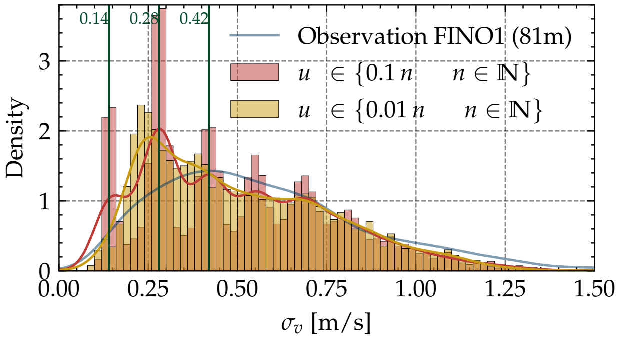

Figure 11. Distribution of σ_v for discretizations of u_* of 0.1 and 0.01 for January and May 2007

A second major source of uncertainty comes from the discretization in bins for microscale time serie generation. Of particular concern is the friction velocity, which is a key scaling parameter in the Cheynet et al. model. It should cover a broad range but while be finely diescretized in the range 0.1-0.3m/s. As uniform discretization was used (see Table 1), an excessively coarse resolution of 0.1m/s was chosen not to blow up computational cost. A sensitivity study is presented in Figure 11, where it is seen that decreasing resolution to 0.01 m/s effectively reduced battlement.

Uncertainties from the wind speed discretizations would also likely contribute to the uncertainty as it is also the principal scaling factor for the frequency of the Cheynet et al. normalized wind spectrum.

The contribution of the bins used for the atmospheric stability would participate differently as the bins are much larger. The main issue there would be to have the spectrum in the wrong stability bin which is possible with the over unstable behavior of the NORA3 hindcast.

From Figure 5, we can note that on a very long 2-year time series, the battlements are much stronger for v and w maybe linked to the use of the Kaimal et al. spectrum for these components.

To the author's knowledge there is no more detailed definition of turbulence intensity other than in IEC 61400-1 (International Electrotechnical Commission, 2019). In particular, the highest frequency of interest (depending on Nyquist and hence sampling frequency) is not defined. While this is not a problem within this study as observations are filtered to match the highest simulated frequency, it makes it hard to relate to other work which may use a larger range.

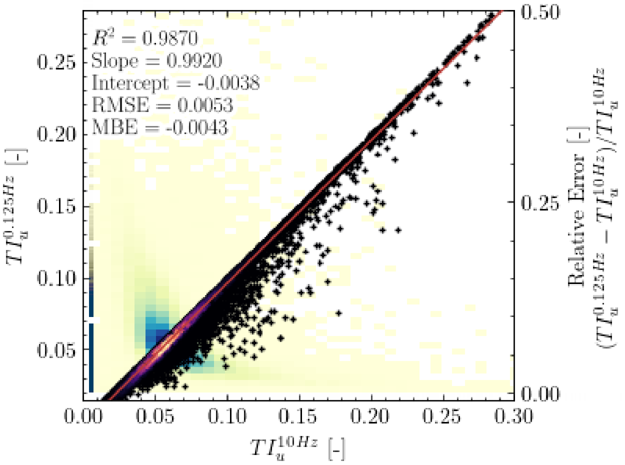

Figure 12. Comparison and relative error between the turbulence intensity observation at FINO1 81m sample at 10Hz (raw) and filtered at 0.125Hz (flaggturb highest frequency).

To illustrate this, Figure 12 compares TI_u obtained by keeping the original 10Hz signal against low-pass filtering it at 0.125Hz. A RMSE of 0.0053 and a MBE of -0.0043 is obtained, corresponding to about 25% of the error measured if the Butterworth low pass filter at 0.125Hz was not applied. It is important to note than the relative error in TI is in general lower than 10%, but can in some situation become as high as 45-50%. It would be valuable to define standard methods for computing the turbulence intensity depending on frequency range of interest, perhaps by filtering any high frequency measurement to 0.5Hz corresponding to the minimum sampling frequency of 1s suggested by IEC 61400-1.

4.2 On spectral representation

The first important point of discussion regarding the spectral representation concerns the atmospheric stability for the low-frequency component of turbulence. As demonstrated by Cheynet et al., the mesoscale component of turbulence varies with atmospheric stability, which is crucial to consider, unlike the approach taken by Larsén et al. (2016). Here, we represent the spectrum for stable, neutral, and unstable conditions in Figure 10, as our objective is to validate whether the generated spectrum aligns with the observed one.

The fitted parameters in the equation of Larsén et al. (2013), also shown in the same figure, exhibit minimal variation across the three stability conditions. The parameters of the $-5/3$ power law section of the spectrum in the low-frequency range are consistent with those reported by Larsén et al. (2016), specifically $3 \times 10^{-4}\,\mathrm{m^2 s^{-8/3}}$. However, for the lowest part of the mesoscale range, extending up to one day and following a -3 power law, we observe an order-of-magnitude difference in the coefficient a_4 compared to the value of 3×10^{-11} $\mathrm{m^2 s^{-4}}$ provided by Larsén et al. (2016). This discrepancy may reflect the local characteristics of the wind spectrum.

Regarding the spectral form itself, it is noteworthy that no spectral gap or microscale peak is observed, which aligns with the findings of Larsén et al. (2016). In their study, 2D mesoscale turbulence dominated at heights such as 80 m and 100 m, a phenomenon also documented by Syed and Mann (2024b). This excess power density was also reported when considering power fluctuation of wind farm by Sørensen et al. (2007).

4.3 On the turbulence model

Bridging the gap between the high-frequency (3D) spectrum and the beginning of the mesoscale (2D) spectrum has been identified as important when considering structural loads and power fluctuations (Sathe et al., 2013; De Maré and Mann, 2014; Sørensen et al., 2007). Recently, various solutions have been proposed, following either the Kaimal et al. spectrum and Veers method, as seen in Larsén et al. (2013); Cheynet et al. (2018), or the Mann model, as in Syed and Mann (2024a, b).

These two approaches are very different, based on time-dependent spectrum for the former and space-dependent wind structure for the latter. While the Mann model has been widely adopted for turbine-level simulations for its closer-to-physics approach, the Veers methods offers numerous advantages for large wind farms (Chabaud, 2024a), a major one being the ability to lift Taylor's frozen turbulence assumption, which is crucial to model the along-wind evolution of mesoscale fluctuations.

A second advantage lies in the input parameters used for the mesoscale (2D) turbulence. In the approach from Cheynet et al., the only required parameters are u_*, u, and z/L, which are easily available using a weather model. On the other hand, the parameters introduced in Syed and Mann (2024b) need to be fitted to in-situ observations (σ^2_{2D}, ψ) or chosen arbitrarily high (L_{2D}). In the method suggested in this paper, an hybrid approach is used, following the method of Larsén et al. and Cheynet et al. by fitting the a_4 parameter (synoptic parameter) on available hindcast or reanalysis data, but fixing the parameter $a_3 = 3 \times 10^{-4}$ $\mathrm{m^2 s^{-8/3}}$, which shows little variability across different offshore and onshore sites, as shown in Figure 10 compared to Larsén et al. (2016). There, it is also worth noting that the approach used of Cheynet et al. scales the entire spectra by the friction velocity and height, including the mesoscale part. This is discussable, as this scaling is valid only for part of the flow for $10^{-4} < f < 10^{-2}$ and will not be valid for lower frequencies, as pointed out by Smedman-Högström and Högström (1975). A recommended approach would be to use scaled spectra for purely microscale turbulence, then add the mesoscale part fitted on unscaled spectra.

5 Conclusions

In this study, a new methodology has been developed for generating long turbulent wind time series by combining mesoscale data from the NORA3 model with microscale spectra from Cheynet et al., using the Gaussian process generation method from Veers; Sørensen et al.; Chabaud. The approach involves using the NORA3 hindcast model to provide mesoscale forcing data, which is then combined with the Cheynet et al. spectrum to capture microscale turbulence. The validation process, using observational data from the FINO1 weather mast, shows a good estimation of wind statistics and spectral representation for periods between 2 minutes and 24 hours.

The main results indicate that the along-wind turbulence intensity is within a confidence interval at 85% of ± 0.02 for 2-hour simulations, with better performance in stable conditions. The model also shows good spectral representation, although there are some limitations in the spectral gap between NORA3's Nyquist frequency and the microscale range, which can be addressed by adding a mesoscale term in the microscale model as suggested by Larsén et al. (2013).

The discussion highlights several key points. First about the error in the estimation of the turbulence intensity, which can be improved by better discretization of the mesoscale forcing data as well as careful filtering of the data to ensure a common comparison basis for the turbulence intensity —the latter missing a standard calculation method to ensure meaningful comparison. Second, the spectral gap (which is shown to be absent offshore) and its modelling have been addressed. Finally, a discussion about the suitability of the suggested method compared to other state-of-the-art models has been given.

In conclusion, the presented methodology offers a promising approach for generating long turbulent wind time series with good statistical and spectral properties. The use of a forecast mesoscale model instead of a hindcast model could further enhance the applicability of this method for near real-time forecasting of the turbulence field and intensity for wind farms. However, the lack of a standard framework for turbulence intensity remains a challenge that needs to be addressed to improve the accuracy and reliability of wind turbulence modeling. This methodology opens new possibilities for the modeling of turbulence intensity and has potential applications in wind farm design and operation, fatigue damage assessment, and wind farm control strategies.

Code and data availability. To generate the time series used in this paper the Julia software FarmStreamV2 connected to FLAggTurb have been used. The configuration is available in the example from FarmStreamV2 https://gitlab.sintef.no/ser-windfarmtools/farmstream/-/tree/main/examples/flaggturb_splicing_wind?ref_type=heads. FLAggTurb is available at https://gitlab.sintef.no/ser-windfarmtools/flaggturb. The code to generate the differents figures is available at Pauchet (2026) (https://doi.org/10.5281/zenodo.18621658). The data used for the validation at FINO1 are available at Pauchet et al. (2025) (https://doi.org/10.60609/B9T9-0X55).

Appendix A

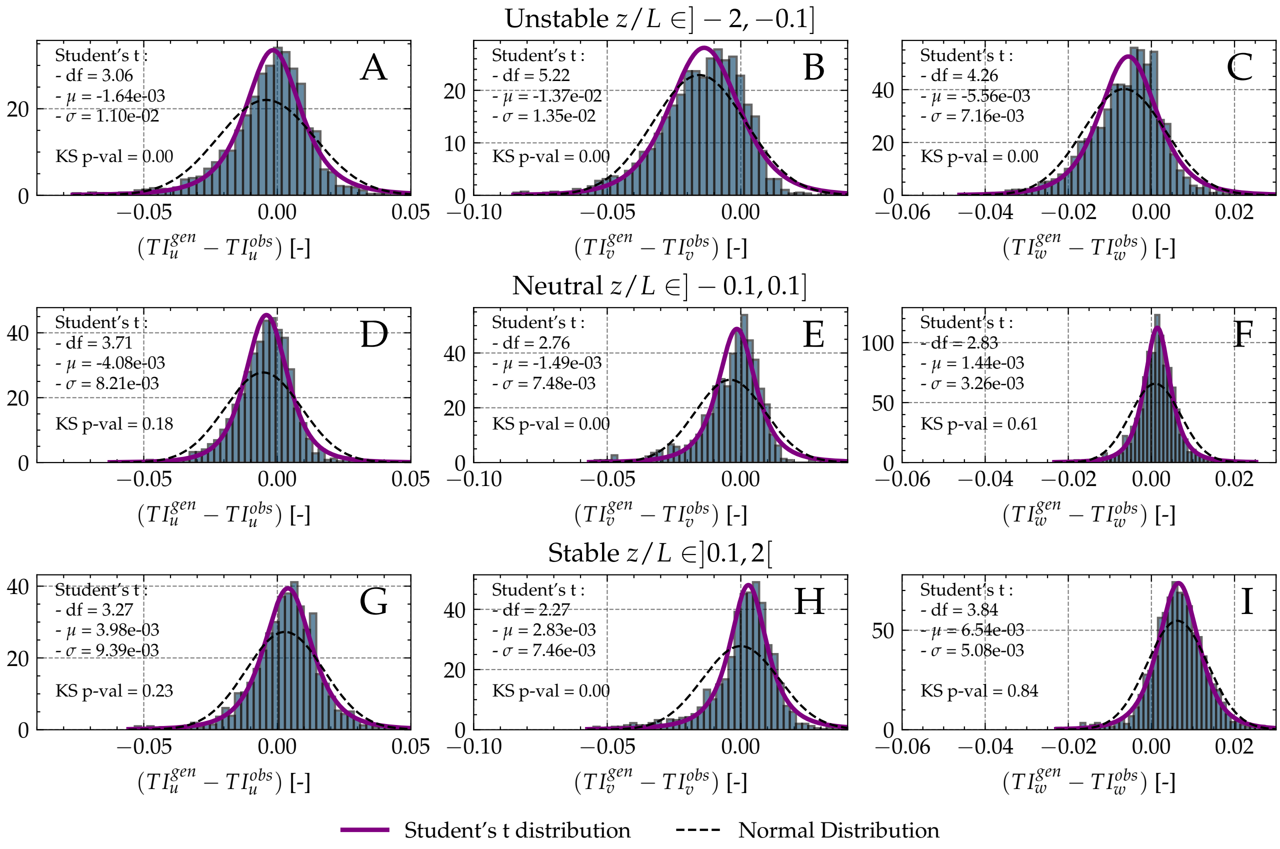

Figure A1. Distribution of the mean error (ME) of TI_u, TI_v, and TI_w for unstable ($z/L \in]-2,-0.1]$), neutral ($z/L \in]-0.1,0.1]$), and stable ($z/L \in]0.1,2[$) conditions. The student's t law is fitted on the distribution with the parameters given.

Author contributions. VC for the conceptualization of the splicing methodology, LP implementation of the methodology for wind fluctuations, and prepared the first draft of the manuscript reviewed and corrected by VC, MBP and LP

Financial support. This work has been accomplished within the EU/HEU WILLOW project, funded by the European Union's Horizon Europe research and innovation programme under grant agreement No. 1011122184.

Competing interests. The authors declare that they have no competing interests

Acknowledgements. We would like to acknowledge the support of Dr. Beatriz Cañadillas from TU Braunschweig, Martin Moritz from the Federal Maritime and Hydrographic Agency, and Jan Niklas Sick from Fachhochschule Kiel GmbH for their indispensable assistance in accessing data from the FINO1 meteorological mast.

We would also like to thank Manuel Siebert from ForWind – Center for Wind Energy Research for providing us with the beautiful picture of FINO1 for the methodology section of this paper.

We are grateful to Jakob Mann, Etienne Cheynet, and Julia Gottschall for their valuable input during, before, and after the EERA Deep-Wind 2026 conference.

This work was partially conducted as part of the end-of-study internship of Louis Pauchet, and we would like to acknowledge the supervision of Abdellah Hadjadj from INSA Rouen Normandie.

The authors used Le Chat (Mistral AI) and Copilot (Microsoft) for phrasing, spelling, and programming assistance. All LLM-generated content was reviewed and validated by the authors, who assume full responsibility for the accuracy and integrity of the final work. No sensitive data were shared with the model.

References

Petroleum and natural gas industries – Specific requirements for offshore structures – Part 1: Metocean design and operating considerations, https://www.iso.org/standard/60183.html, 2015.

Bengtsson, L., Andrae, U., Aspelien, T., Batrak, Y., Calvo, J., De Rooy, W., Gleeson, E., Hansen-Sass, B., Homleid, M., Hortal, M., Ivarsson, K.-I., Lenderink, G., Niemelä, S., Nielsen, K. P., Onvlee, J., Rontu, L., Samuelsson, P., Muñoz, D. S., Subias, A., Tijm, S., Toll, V., Yang, X., and Koltzow, M. O.: The HARMONIE–AROME Model Configuration in the ALADIN–HIRLAM NWP System, Monthly Weather Review, 145, 1919–1935, https://doi.org/10.1175/mwr-d-16-0417.1, publisher: American Meteorological Society, 2017.

Bundesamt für Seeschifffahrt und Hydrographie (BSH): FINO1 Metadata, Tech. rep., Bundesamt für Seeschifffahrt und Hydrographie (BSH), https://www.bsh.de/DE/THEMEN/Beobachtungssysteme/Messnetz-MARNET/FINO/_Anlagen/Downloads/FINO1_metadata.pdf?__blob=publicationFile&v=2, accessed: 2025-11-03, 2015.

Chabaud, V.: FLAggTurb, https://gitlab.sintef.no/valentin.chabaud/flaggturb, 2023.

Chabaud, V.: Synthetic turbulence modelling for offshore wind farm engineering models using coherence aggregation, Wind Energy, 27, 111–130, https://doi.org/10.1002/we.2875, 2024a.

Chabaud, V.: Power Fluctuations caused by Wind Turbulence on a 15MW Floating Offshore Wind Turbine, Project Memo AN 24.12.22, Sintef Energy Research, https://hdl.handle.net/11250/3169507, 2024b.

Chabaud, V.: A Quantification of Power Fluctuations from Generic Offshore Wind Farms, in: Journal of Physics: Conference Series, vol. 3131, p. 012015, IOP Publishing, 2025.

Cheynet, E., Jakobsen, J. B., and Reuder, J.: Velocity Spectra and Coherence Estimates in the Marine Atmospheric Boundary Layer, Boundary-Layer Meteorology, 169, 429–460, https://doi.org/10.1007/s10546-018-0382-2, 2018.

Christakos, K., Bjermeland, L., efvik, annks, Furevik, B. R., and Pauchet, L.: metocean-api, https://github.com/MET-OM/metocean-api, 2024.

Copernicus Climate Change Service: ERA5 hourly data on pressure levels from 1940 to present, https://doi.org/10.24381/CDS.BD0915C6, 2018.

De Maré, M. and Mann, J.: Validation of the Mann spectral tensor for offshore wind conditions at different atmospheric stabilities, Journal of Physics: Conference Series, 524, 012 106, https://doi.org/10.1088/1742-6596/524/1/012106, 2014.

Foken, T., Göockede, M., Mauder, M., Mahrt, L., Amiro, B., and Munger, W.: Post-Field Data Quality Control, in: Handbook of Micrometeorology, edited by Lee, X., Massman, W., and Law, B., vol. 29, pp. 181–208, Kluwer Academic Publishers, Dordrecht, ISBN 978-1-4020-2264-7, https://doi.org/10.1007/1-4020-2265-4_9, series Title: Atmospheric and Oceanographic Sciences Library, 2005.

Fratini, G. and Mauder, M.: Towards a consistent eddy-covariance processing: an intercomparison of EddyPro and TK3, Atmospheric Measurement Techniques, 7, 2273–2281, https://doi.org/10.5194/amt-7-2273-2014, 2014.

Haakenstad, H., Breivik, O., Furevik, B. R., Reistad, M., Bohlinger, P., and Aarnes, O. J.: NORA3: A Nonhydrostatic High-Resolution Hindcast of the North Sea, the Norwegian Sea, and the Barents Sea, Journal of Applied Meteorology and Climatology, 60, 1443–1464, https://doi.org/10.1175/JAMC-D-21-0029.1, 2021.

Hersbach, H., Bell, B., Berrisford, P., Hirahara, S., Horányi, A., Muñoz-Sabater, J., Nicolas, J., Peubey, C., Radu, R., Schepers, D., Simmons, A., Soci, C., Abdalla, S., Abellan, X., Balsamo, G., Bechtold, P., Biavati, G., Bidlot, J., Bonavita, M., De Chiara, G., Dahlgren, P., Dee, D., Diamantakis, M., Dragani, R., Flemming, J., Forbes, R., Fuentes, M., Geer, A., Haimberger, L., Healy, S., Hogan, R. J., Hólm, E., Janisková, M., Keeley, S., Laloyaux, P., Lopez, P., Lupu, C., Radnoti, G., De Rosnay, P., Rozum, I., Vamborg, F., Villaume, S., and Thépaut, J.: The ERA5 global reanalysis, Quarterly Journal of the Royal Meteorological Society, 146, 1999–2049, https://doi.org/10.1002/qj.3803, 2020.

Hoyer, S. and Hamman, J.: xarray: N-D labeled Arrays and Datasets in Python, Journal of Open Research Software, 5, 10, https://doi.org/10.5334/jors.148, 2017.

Högström, U., Hunt, J. C. R., and Smedman, A.-S.: Theory And Measurements For Turbulence Spectra And Variances In The Atmospheric Neutral Surface Layer, Boundary-Layer Meteorology, 103, 101–124, https://doi.org/10.1023/A:1014579828712, 2002.

International Electrotechnical Commission, ed.: Design requirements, no. part 1 in Wind energy generation systems / International Electrotechnical Commission, International Electrotechnical Commission, Geneva, Switzerland, edition 4.0 edn., ISBN 978-2-8322-6253-5, 2019.

Jeans, G.: Converging profile relationships for offshore wind speed and turbulence intensity, Wind Energy Science, 9, 2001–2015, https://doi.org/10.5194/wes-9-2001-2024, 2024.

Jonkman, B. J.: TurbSim User's Guide: Version 1.50, Technical Report NREL/TP-500-46198, National Renewable Energy Laboratory, 2009.

Kaimal, J. C. and Finnigan, J. J.: Atmospheric boundary layer flows: their structure and measurement, Oxford university press, 1994.

Kaimal, J. C., Wyngaard, J. C., Izumi, Y., and Coté, O. R.: Spectral characteristics of surface-layer turbulence, Quarterly Journal of the Royal Meteorological Society, 98, 563–589, https://doi.org/10.1002/qj.49709841707, 1972.

Larsén, X. G., Vincent, C., and Larsen, S.: Spectral structure of mesoscale winds over the water, Quarterly Journal of the Royal Meteorological Society, 139, 685–700, https://doi.org/10.1002/qj.2003, 2013.

Larsén, X. G., Larsen, S. E., and Petersen, E. L.: Full-Scale Spectrum of Boundary-Layer Winds, Boundary-Layer Meteorology, 159, 349–371, https://doi.org/10.1007/s10546-016-0129-x, 2016.

LI-COR Biosciences: Eddy Covariance Processing Software (Version 7.0.8), www.licor.com/EddyPro, 2021.

LI-COR Biosciences: EddyPro Software Instruction Manual (Version 7.0), LI-COR, Inc., Lincoln, Nebraska, USA, https://www.licor.com/env/products/eddy_covariance/eddypro.html, version Number: 7.0, 2023.

Mann, J.: The spatial structure of neutral atmospheric surface-layer turbulence, Journal of Fluid Mechanics, 273, 141–168, https://doi.org/10.1017/S0022112094001886, 1994.

Mann, J.: Wind field simulation, Probabilistic Engineering Mechanics, 13, 269–282, https://doi.org/10.1016/S0266-8920(97)00036-2, 1998.

Masson, V., Le Moigne, P., Martin, E., Faroux, S., Alias, A., Alkama, R., Belamari, S., Barbu, A., Boone, A., Bouyssel, F., Brousseau, P., Brun, E., Calvet, J.-C., Carrer, D., Decharme, B., Delire, C., Donier, S., Essaouini, K., Gibelin, A.-L., Giordani, H., Habets, F., Jidane, M., Kerdraon, G., Kourzeneva, E., Lafaysse, M., Lafont, S., Lebeaupin Brossier, C., Lemonsu, A., Mahfouf, J.-F., Marguinaud, P., Mokhtari, M., Morin, S., Pigeon, G., Salgado, R., Seity, Y., Taillefer, F., Tanguy, G., Tulet, P., Vincendon, B., Vionnet, V., and Voldoire, A.: The SURFEXv7.2 land and ocean surface platform for coupled or offline simulation of earth surface variables and fluxes, Geoscientific Model Development, 6, 929–960, https://doi.org/10.5194/gmd-6-929-2013, 2013.

May, R., Arms, S., Marsh, P., Bruning, E., Leeman, J., Bruick, Z., and Camron, M. D.: MetPy: A Python Package for Meteorological Data, https://doi.org/10.5065/D6WW7G29, language: en, 2016.

Pauchet, L.: LouisPauchet/Long_Wind_Time_Series_Processing_Notebooks: 0.0, https://doi.org/10.5281/ZENODO.18621658, 2026.

Pauchet, L. and Chabaud, V.: Synthetic Wind Modeling, Prosjektnotat PN25-00111, SINTEF Energi AS, https://hdl.handle.net/11250/5332625, 2025.

Pauchet, L., Chabaud, V., and SINTEF Energy Research: Wind speed and direction, Atmospheric Stability, Turbulence Intensity, Turbulent Kinetic Energy and Sensible Heat Fluxes in the North Sea (FINO1), https://doi.org/10.60609/B9T9-0X55, 2025.

https://doi.org/10.5194/wes-2026-58
Preprint. Discussion started: 10 April 2026

Sadeghi, N., Robbelein, K., D'Antuono, P., Noppe, N., Weijtjens, W., and Devriendt, C.: Fatigue damage calculation of offshore wind turbines' long-term data considering the low-frequency fatigue dynamics, Journal of Physics: Conference Series, 2265, 032 063, https://doi.org/10.1088/1742-6596/2265/3/032063, 2022.

Sadeghi, N., D'Antuono, P., Noppe, N., Robbelein, K., Weijtjens, W., and Devriendt, C.: Quantifying the effect of low-frequency fatigue dynamics on offshore wind turbine foundations: a comparative study, Wind Energy Science, 8, 1839–1852, https://doi.org/10.5194/wes-8-1839-2023, 2023.

Sathe, A., Mann, J., Barlas, T., Bierbooms, W., and Van Bussel, G.: Influence of atmospheric stability on wind turbine loads, Wind Energy, 16, 1013–1032, https://doi.org/10.1002/we.1528, 2013.

Smedman-Högström, A.-S. and Högström, U.: Spectral Gap in Surface-Layer Measurements, Journal of the Atmospheric Sciences, 32, 340–350, https://doi.org/10.1175/1520-0469(1975)032<0340:SGISLM>2.0.CO;2, 1975.

Solbrekke, I. M., Sorteberg, A., and Haakenstad, H.: The 3 km Norwegian reanalysis (NORA3) – a validation of offshore wind resources in the North Sea and the Norwegian Sea, Wind Energy Science, 6, 1501–1519, https://doi.org/10.5194/wes-6-1501-2021, 2021.

St. Pé, A., Weyer, E., Campbell, I., Arntsen, A. E., Kondabala, N., Mibus, M., Coulombe-Pontbriand, P., Black, A. H., Parker, Z., Swytink-Binnema, N., Jolin, N., Goudeau, B. T., Meklenborg Miltersen Slot, R., Svenningsen, L., Lee, J. C. Y., Debnath, M., Wylie, S., Apgar, D., Fric, T., Michaud, D., Smith, E., Mazoyer, P., Tocco, M., Guillemin, F., Teoh, K., and Meyers, M.: CFARS Site Suitability Initiative: An Open Source Approach to Evaluate the Performance of Remote Sensing Device (RSD) Turbulence Intensity Measurements & Accelerate Industry Adoption of RSDs for Turbine Suitability Assessment, https://doi.org/10.5281/ZENODO.5529750, publisher: Zenodo, 2021.

Syed, A. H. and Mann, J.: A Model for Low-Frequency, Anisotropic Wind Fluctuations and Coherences in the Marine Atmosphere, Boundary-Layer Meteorology, 190, 1, https://doi.org/10.1007/s10546-023-00850-w, 2024a.

Syed, A. H. and Mann, J.: Simulating low-frequency wind fluctuations, Wind Energy Science, 9, 1381–1391, https://doi.org/10.5194/wes-9-1381-2024, 2024b.

Sørensen, P., Hansen, A. D., and Rosas, P. A. C.: Wind models for simulation of power fluctuations from wind farms, Journal of Wind Engineering and Industrial Aerodynamics, 90, 1381–1402, https://doi.org/10.1016/S0167-6105(02)00260-X, 2002.

Sørensen, P., Cutululis, N. A., Vigueras-Rodriguez, A., Jensen, L. E., Hjerrild, J., Donovan, M. H., and Madsen, H.: Power Fluctuations From Large Wind Farms, IEEE Transactions on Power Systems, 22, 958–965, https://doi.org/10.1109/TPWRS.2007.901615, 2007.

Van Der Hoven, I.: Power spectrum of horizontal wind speed in the frequency range from 0.0007 to 900 cycles per hour, Journal of Meteorology, 14, 160–164, https://doi.org/10.1175/1520-0469(1957)014<0160:PSOHWS>2.0.CO;2, 1957.

Veers, P.: Three-Dimensional Wind Simulation, 1988.

Veers, P., Dykes, K., Lantz, E., Barth, S., Bottasso, C. L., Carlson, O., Clifton, A., Green, J., Green, P., Holttinen, H., Laird, D., Lehtomäki, V., Lundquist, J. K., Manwell, J., Marquis, M., Meneveau, C., Moriarty, P., Munduate, X., Muskulus, M., Naughton, J., Pao, L., Paquette, J., Peinke, J., Robertson, A., Sanz Rodrigo, J., Sempreviva, A. M., Smith, J. C., Tuohy, A., and Wiser, R.: Grand challenges in the science of wind energy, Science, 366, eaau2027, https://doi.org/10.1126/science.aau2027, 2019.

Vigueras-Rodríguez, A., Sørensen, P., Viedma, A., Donovan, M., and Gómez Lázaro, E.: Spectral coherence model for power fluctuations in a wind farm, Journal of Wind Engineering and Industrial Aerodynamics, 102, 14–21, https://doi.org/10.1016/j.jweia.2011.12.006, 2012.